

Check for updates

Ferroelectric-Gated Hybrid-Layered Organic Field-Effect **Transistors for Multimode Signal Processing**

Jie Liu, Mengyun Zhang, Wushuang Han, Fan Du, Limin Wu,* and Xiaosheng Fang*

The rapid development of intelligent systems has driven the urgent need for multifunctional devices within a unified framework through innovative design principles. Here, a ferroelectric-gated organic field-effect transistor (Fe-OFET) is proposed, which synergistically combines light perception, data storage, and neuromorphic computing functionalities. The device features a hybrid-layered channel with engineered organic molecule modification, improving photodetection performance via optimized exciton dissociation, electron trapping, and hole injection. This design yields exceptional photoresponsivity of 2.4 A W^{-1} and detectivity of 1.3 \times 10¹³ Jones. Integration of the ferroelectric layer enables nonvolatile conductance modulation, exhibiting a wide memory window, robust switching endurance with an on/off ratio of $>10^4$ and long-term data retention exceeding 4×10^3 s. Furthermore, the Fe-OFET-based synapse architecture demonstrates potential for wearable neuromorphic electronics, combining flexibility with cognitive functions. The device demonstrates accurate recognition and classification of electrocardiogram waveforms and handwritten digits, achieving accuracies up to 85% and 91%, respectively. This work establishes a hardware paradigm in multimode signal processing and adaptive edge intelligence, offering innovative solutions for next-generation electronics targeting diverse application scenarios.

1. Introduction

Advancements in artificial intelligence have driven unprecedented demand for hardware architectures capable of processing and storing information with high efficiency. Conventional architectures mostly rely on a combination of various components and logic circuits.^[1] This approach introduces a limitation that the physical separation between units restricts information exchange, leading to slower processing and reduced energy

J. Liu, M. Zhang, W. Han, F. Du, L. Wu, X. Fang College of Smart Materials and Future Energy and State Key Laboratory of

Molecular Engineering of Polymers

Fudan University

Shanghai 200438, P. R. China

E-mail: lmw@fudan.edu.cn; xshfang@fudan.edu.cn

College of Chemistry and Chemical Engineering Inner Mongolia University

Hohhot 010021, P. R. China

The ORCID identification number(s) for the author(s) of this article can be found under https://doi.org/10.1002/adfm.202508765

DOI: 10.1002/adfm.202508765

efficiency.[2] To address these challenges, integrating sensing, storage, and neuromorphic computing capabilities has emerged as a new strategy, aiming to unify sensor, memory, and processing units within a single device. [3-5] This integration simplifies system architecture, improves area efficiency, and minimizes power consumption.

Recently, researchers have focused on developing integrated devices capable of performing multi-signal processing.[6-8] Artificial synapses have demonstrated the capability to replicate biological synaptic characteristics, offering potential applications in perception, memory, and neural computing.^[9-11] Synaptic weight is updated through electrical and/or optical pulse stimulation, thereby establishing connections between external stimuli and neural networks.[12-15] In a significant advancement, a two-terminal optoelectronic resistive random access memory synaptic device that exhibits nonvolatile optical resistive switching and lighttunable synaptic behaviors, specifically designed for a neuromorphic visual system, was developed.[16] Reconfigurable devices,

which can dynamically alter their functions during operation to accomplish different tasks, have emerged as promising alternatives for enhancing integration level and reducing power consumption in next-generation electronics.^[17–20] The construction of multifunctional optoelectronic devices through controlled absorption and desorption of gas molecules on the channel was demonstrated. The field-effect transistor achieved multiple functions, including photodetection, memory, Boolean logic operations, and artificial synapses.[21] Photomemristors represent another category of multifunctional devices that provide superior decoupling between stimuli and status-reading electrical pathways, enabling independent optimization of each functional layer.[22,23] A nonvolatile photomemristor was proposed wherein reconfigurable responsivity can be modulated and stored through charge and/or photon flux manipulation.^[24] These devices, which process both electrical and optical signals, represent a significant advancement in creating versatile, multifunctional electronic and optoelectronic systems. Organic ferroelectric transistors incorporating polymeric dielectrics and organic semiconductors demonstrate significant potential because they combine multi-domain polarization switching with several advantageous characteristics: inherent flexibility, biocompatibility, low power consumption, and tunable photoelectrical properties.

16163028, 0, Downloaded from https://advanced.onlinelibrary.wiley.com/doi/10.1002/adfm.022508765 by Fudatu University, Wiley Online Library on [28.09/2025]. See the Terms and Conditions (https://onlinelibrary.wiley.com/terms-and-conditions) on Wiley Online Library for rules of use; OA arctices are governed by the applicable Creative Commons Licenses

Figure 1. Integrated multimode signal processing system for signal sensing, nonvolatile memory, and neuromorphic computing based on Fe-OFETs. The Fe-OFET architecture consists of PC₇₁BM doped C8-BTBT, MoO₃, CB-BTBT, and P(VDF-TrFE), which are corresponding to photoactive layer, hole transport layer, conduction layer, ferroelectric layer.

These features make them particularly suitable for both largescale integration and wearable electronic applications.^[25–28]

In this study, we demonstrate a ferroelectric-gated organic field-effect transistor (Fe-OFET) that integrates signal sensing, information storage, and neuromorphic computing functionalities. For photodetection, [6,6]-phenyl-C71-butyric acid methyl ester (PC₇₁BM), an electron acceptor, was introduced into 2,7dioctyl[1]-benzothieno[3,2-b][1]benzothiophene (C8-BTBT) photoactive layer to optimize exciton dissociation and electron trapping. An ultrathin inorganic molybdenum trioxide (MoO₂) interlayer, acting as a hole transport medium, facilitates hole injection while suppressing electron-hole recombination. This hybridlayered architecture achieves high responsivity (2.4 A W⁻¹) and detectivity (1.3 × 10¹³ Jones) under 350 nm ultraviolet illumination. For non-volatile memory, the incorporated ferroelectric gate dielectric enables non-volatile conductance modulation, exhibiting a wide memory window, robust switching endurance (on/off ratio of >10⁴), and prolonged retention time (>4 \times 10³). Notably, we demonstrated the application of Fe-OFET as a wearable, intelligent healthcare device capable of real-time diagnosis through the processing of complex electrocardiogram (ECG) signals from patients with arrhythmia. Meanwhile, the recognition accuracy of Modified National Institute of Standards and Technology (MNIST) patterns based on an artificial neural network (ANN) model reached 91%. These results indicate the prospect of Fe-OFET-based synapse architecture in neuromorphic electronics. The work establishes a new paradigm for multimode signal processing, offering innovative solutions for diverse application scenarios.

2. Results and Discussion

2.1. Integrated Multimode Signal Processing System

Figure 1 illustrates the proposed Fe-OFET multimode signal processing system, which seamlessly integrates signal sensing,

nonvolatile memory, and intelligent processing of complex sequential bio-signals. The high-sensitivity optical sensing utilizes an organic hybrid-layered architecture to enhance exciton dissociation and carrier transport, significantly improving photodetection performance. The non-volatile electrical signals memory, reminiscent of the human brain's memory system, stores electrical signals with fidelity. Remarkably, even after mechanical bending, the device retains the capability to read and write logic signals. The bionic neural network processing features an ANN architecture with 187 input neurons, 128 hidden neurons, and 5 output neurons, forming a fully connected network. This ANN model is employed in processing ECG signals such as arrhythmias and obstructive sleep apnea, when measured in realtime through edge devices. The schematic diagram of hybridlayered Fe-OFETs is shown on the right side of Figure 1. The detailed preparation process for the multilayer heterostructure is described in the Experimental Section and illustrated in Figure S1 (Supporting Information). In brief, the ferroelectric polymer poly(vinylidene fluoride-trifluoroethylene) (P(VDF-TrFE)) serves as the gate dielectric layer, prepared via spin coating. Nonvolatile and rewritable characteristics of ferroelectric polarization lay the foundation for state switching and retention of Fe-OFET.[29-33] The organic hybrid-layered architecture was designed to optimize the optical detection performance of the devices. Meanwhile, it offers advantages of flexibility, lightweight properties, and low-cost production, making it suitable for wearable devices.

2.2. Spectral and Micromorphological Characterizations

The XRD pattern of the C8-BTBT film deposited on the P(VDF-TrFE) layer, shown in **Figure 2a**, reveals its crystalline structure (Figure S2, Supporting Information). Diffraction peaks at 6.04° and 9.08°, corresponding to the (002) and (003) lattice planes, respectively, can be assigned to the (00l) plane family of C8-BTBT.^[34] Similar patterns were also observed in the improved

16163028, 0, Downloaded from https://advanced.onlinelibrary.wiley.com/doi/10.1002/adfm.202508765 by Fudan University, Wiley Online Library on [28.092025]. See the Terms and Conditions (https://onlinelibrary.wiley.com/term

and-conditions) on Wiley Online Library for rules of use; OA articles are governed by the applicable Creative Commons License

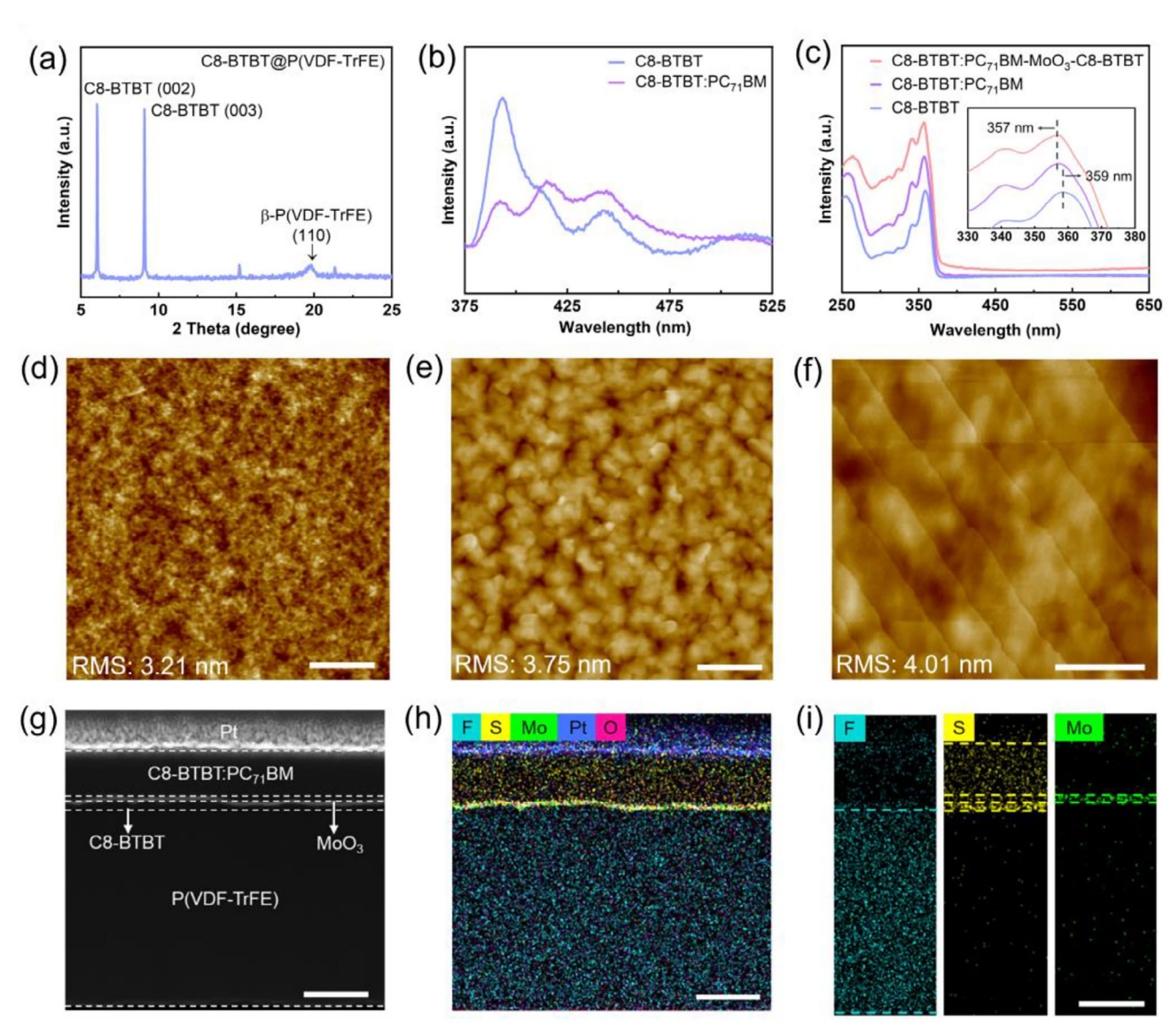


Figure 2. a) XRD pattern of C8-BTBT/P(VDF-TrFE) bi-layered film. b) PL spectra of C8-BTBT and C8-BTBT:PC₇₁BM films. c) Absorption spectra of different multilayer films on a quartz substrate. AFM images of d) P(VDF-TrFE) film, e) C8-BTBT film, and f) C8-BTBT:PC₇₁BM film. scale bar, 2 µm. g) Cross-sectional TEM images of a vertically stacked C8-BTBT:PC₇₁BM/MoO₃/CB-BTBT/P(VDF-TrFE) heterostructure film and h,i) corresponding EDS element mapping, showing the distribution of F, S, and Mo. Scale bar, 100 nm.

drop-casting C8-BTBT:PC $_{71}$ BM film (Figure S3, Supporting Information). The full widths at half maximum of the (002) and (003) planes are 0.05° and 0.06°, respectively, indicating high crystalline quality and uniform orientation of large-area crystals. Photoluminescence (PL) analysis further highlights the interactions between C8-BTBT and PC $_{71}$ BM molecules (Figure 2b). C8-BTBT absorbs photons while PC $_{71}$ BM traps photoelectrons. The efficient dissociation of excitons and charge transfer between the C8-BTBT and PC $_{71}$ BM molecules reduces electronhole recombination and suppresses the PL quantum yield. Additionally, Förster resonance energy transfer from C8-BTBT to PC $_{71}$ BM molecules may contribute to the suppressed quantum yield as well. Molecules may contribute to the suppressed quantum yield as well. The absorption spectra of the multilayer films share similar profiles, with differences in absorption

intensity (Figure 2c). The typical absorption peak at 359 nm originates from the π -conjugated structure of C8-BTBT. [38,39] However, the incorporation of PC $_{71}$ BM disrupts the intermolecular order of C8-BTBT, shortening its effective conjugation length. This structural alteration results in a slight blue shift of the absorption peak from 359 to 357 nm. [40]

To assess the nanoscale morphological evolution of organic heterojunctions, surface roughness was measured using atomic force microscopy (AFM). The spin-coated P(VDF-TrFE) film exhibits a dense, flat, and smooth surface (RMS = 3.21 nm), providing a high-quality platform for the growth of the conduction layer (Figure 2d). Compared to the C8-BTBT film directly deposited on SiO_2 , the pre-coated P(VDF-TrFE) layer promotes better molecularly ordered assembly and grain connectivity in

16163028, 0, Downloaded from https://advanced.onlinelbtarry.wiley.com/doi/10.1002/adfm.022508765 by Fudau University, Wiley Online Library on [2809/2025]. Sethe Terms and Conditions (https://onlinelibrary.wiley.com/terms-and-conditions) on Wiley Online Library for uses of use; OA arctices are governed by the applicable Creative Commons License

www.afm-journal.de

the C8-BTBT layer due to increased surface wettability (RMS of 3.75 nm in Figure 2e, compared to 6.75 nm in Figure S4, Supporting Information).[41,42] Distinct step-like contour lines in the droplet traces are visible in Figure 2f. To confirm the uniformity of this preparation method for large-scale applications, AFM measurements were performed at three randomly selected positions, showing high morphological consistency and low surface roughness (Figure S5, Supporting Information). AFM imaging of the crystals reveals no observable defects or grain boundaries. The flat surface, with an RMS roughness of 4.01 nm, suggests minimal crystal defects and recombination sites, reducing carrier trapping and enhancing suitability for photoelectric detection applications.[41] Cross-sectional transmission electron microscopy (TEM) imaging and energy-dispersive X-ray spectrometry (EDS) elemental mapping further reveal the multilayer heterostructure of the C8-BTBT:PC71BM/MoO3/C8-BTBT/P(VDF-TrFE) film (Figure 2g-i). A platinum (Pt) top layer was intentionally added during testing to enhance the conductivity of multilayer films. TEM observation confirms a well-defined stacking structure and clear elemental distributions, supporting the development of Fe-OFET devices with low leakage, high endurance, and large-scale uniformity.

2.3. Photoresponse Behaviors and Optical Communication

The optoelectronic behaviors of the hybrid-layered Fe-OFET were systematically studied an atmospheric environment. Figure 3a shows an optical image of the array units fabricated on a flexible polyethylene naphthalate (PEN) substrate. Figure 3b presents the carriers transport paths diagram and energy level diagram. For the photoactive layer, the p-type organic semiconductor C8-BTBT is employed due to its strong light-matter interaction and high charge mobility.[41,42] However, despite its efficient light absorption, the recombination of photogenerated excitons remains a challenge. To address this issue, PC₇₁BM molecules were incorporated into the photoactive layer, forming the C8-BTBT:PC₇₁BM layer. [43,44] In this configuration, C8-BTBT absorbs photons and forms excitons. Acting as an electron acceptor, PC₇₁BM rapidly captures photoexcited electrons from C8-BTBT, promoting efficient exciton dissociation due to the energy offset in the LUMO levels of C8-BTBT and PC71BM and intrinsic electron capture capacity. To further enhance performance, an ultrathin MoO₃ interlayer (≈10 nm) was introduced at the electrodes/C8-BTBT and C8-BTBT:PC71BM/C8-BTBT interfaces (Figure S6, Supporting Information). MoO₃ serves as an interface modification layer, reducing contact resistance and improving hole mobility between the electrodes and the organic semiconductor (Figure S7, Supporting Information).[45] Additionally, its unique charge-selective characteristic blocks electron flow from the photoactive layer to the conduction layer, effectively suppressing electron-hole recombination. [46] Since the photoactive layer was fabricated using a solution-based coating process, the MoO₃ film also functions as a protective barrier, preventing degradation of the underlying conduction layer. The incorporation of an underlying C8-BTBT conduction layer establishes an optimized pathway for channel carrier transport while simultaneously mitigating two critical issues: dielectric screening effect induced by significant dielectric constant mismatch between MoO₃ ($\varepsilon \approx 25$)

and P(VDF-TrFE) ($\epsilon \approx 10$), and crystallographic degradation of ferroelectric layer resulting from high-temperature MoO $_3$ deposition processes. This composite architecture establishes the FeOFET as a highly promising platform for advanced optoelectronic applications, offering improved efficiency, stability, and scalability.

In the non-polarized state, the photo-switching behavior at a wavelength of 350 nm and $V_{ds} = 0.1 \text{ V}$ is illustrated in Figure 3c. Due to the energy level gradient drive and efficient electron trapping in the photoactive layer, exciton dissociation is significantly enhanced, which is reflected in its performance, yielding a higher on/off current ratio (>10³) and a shorter photoresponse time. Additionally, the imaging array demonstrates that the hybrid-layered devices produce sharper and higher-contrast patterns (Figure S8, Supporting Information). The I-V curves under various light power densities were also recorded (Figure 3d). As the increase of incident light power, the channel current rises significantly and saturates at a power density of 1795 µW cm⁻². Both photocurrent (I_{ph}) and I_{ph}/I_{dark} are positively correlated with light power density, and the device retains the ability to distinguish photocurrentdark signals even under weak light conditions (Figure S9, Supporting Information). The device achieves a responsivity (R) of 2.4 A W⁻¹ at a power density of 12 μW cm⁻², in which responsivity is given by $R = I_{\rm ph}/(PA)$, where P is the light power density, and A is the effective area of the device. The high responsivity is primarily attributed to hole reinjection facilitated by the efficient electron trapping of PC₇₁BM doping in the photoactive layer. Additionally, the MoO₃ layer make efforts by functioning as a hole-injecting and electron-blocking layer, further suppressing electron-hole recombination. Another critical parameter, detectivity (D*), reflects the photosensitivity and shot noise limit of photodetector, which can be described as $D^* = RA^{1/2} (2eI_{dark})^{-1/2}$. The device achieves a high D* of up to 1.3×10^{13} Jones under the light power density of 12 µW cm⁻² (Figure 3e). In addition, we summarized the detectivity of organic photodetectors, as shown in Figure 3f. The detectivity of our devices is comparable to those of the best-performing devices, showing an obvious advantage in the ultraviolet range. The more detailed parameters are available in Table S1 (Supporting Information). We also analyze the dependence of detection characteristics on excitation wavelength (Figure 3g; Figure S10, Supporting Information). In the ultraviolet region (250-350 nm), the detector demonstrates excellent photosensitivity, consistent with the light absorption behaviors observed in Figure 2c. However, the device exhibits weak or even negligible response to the excitation light with wavelength exceeding 400 nm, indicating that the intermediate energy levels formed by PC71BM doping primarily trap photogenerated electrons, but have little influence on photon absorption (Figure 3h). Mechanical bending tests are of great significance in evaluating the potential of flexible optoelectronic devices in wearable electronics (Figure 3i; Figure S11, Supporting Information). By adding a poly(methyl methacrylate) (PMMA) coating, the device's bending resistance can be significantly enhanced. After 1000 bending cycles (bending radius: 1 cm, Figure S12, Supporting Information), the photocurrent and on/off ratio of the device can maintain 90.4% and 93.2% of their initial values, respectively. Compared to devices without a PMMA coating, the improvement of photocurrent is particularly notable. The results demonstrate that the PMMA-coated Fe-OFET can

16163208, 0, Downloaded from https://advanced.onlinelibrary.wiley.com/doi/10.1002/adfm.202508765 by Fudau University. Wiley Online Library on [2809/2025]. See the Terms and Conditions (https://onlinelibrary.wiley.com/terms-and-conditions) on Wiley Online Library for rules of use; OA articles are governed by the applicable Creative Commons License

www.afm-journal.de

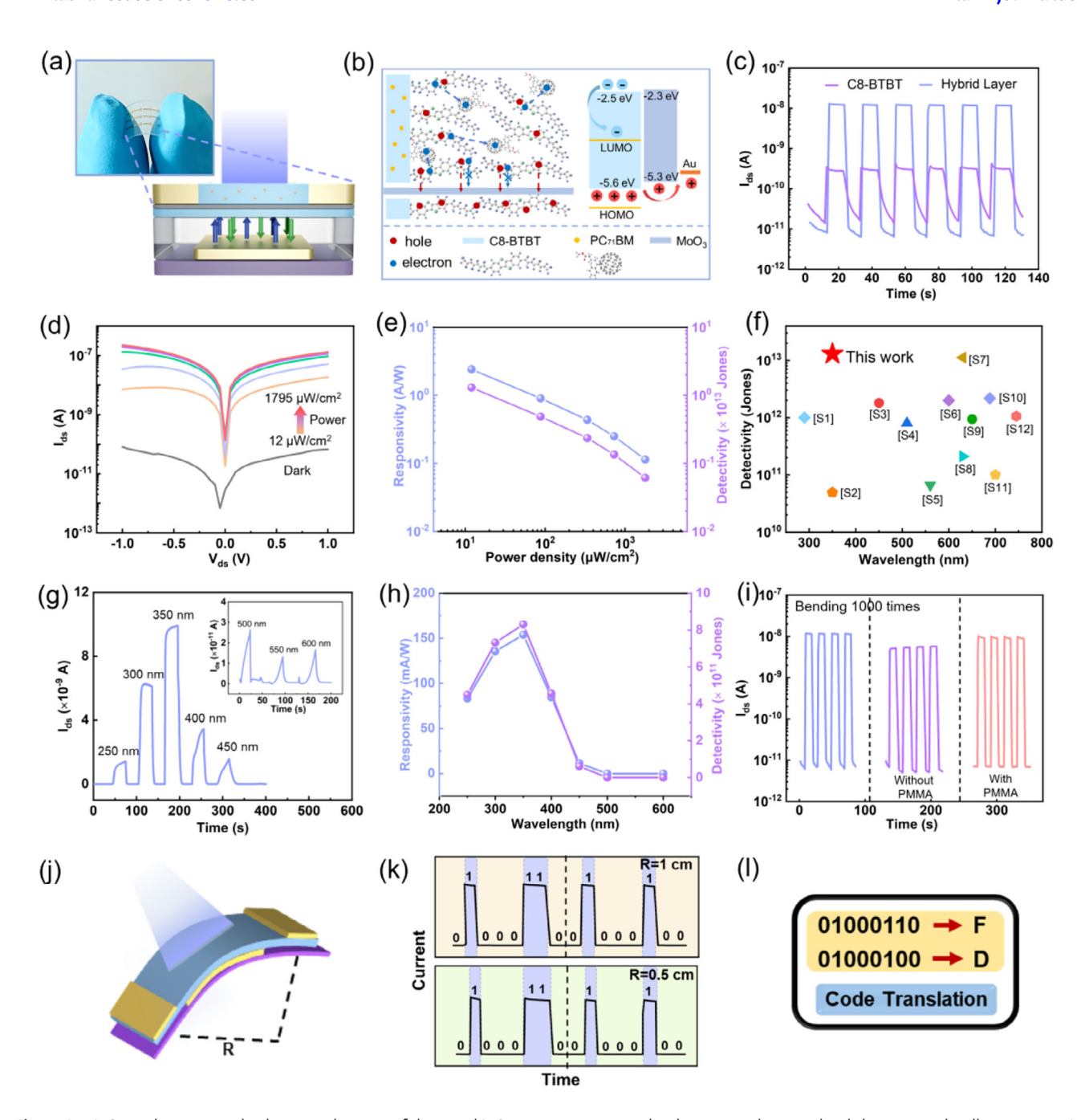


Figure 3. a) Optical picture and schematic diagram of devices. b) Carriers transport paths diagram and energy level diagram under illumination. c) Photoswitching behaviors (I_{ds} -t) of C8-BTBT and hybrid-layer based photodetector (λ = 350 nm, V_{ds} = 0.1 V). d) I_{ds} - V_{ds} curves of the hybrid-layer device under dark and various light power densities from 12 μW cm⁻² to 1795 μW cm⁻². e) The changing tendency of responsivity (R) and detectivity (D*) with the light power density, reaching maximum values of R = 2.4 A W⁻¹, D* = 1.3 × 10¹³ Jones at V_{ds} = 1 V. f) Comparison of detectivity between Fe-OFET with organic photodetectors. g) Photoresponse behaviors (I_{ds} -t) under different wavelengths from 250 to 600 nm. h) The responsivity and detectivity as a function of excitation wavelengths. i) Mechanical stability of Fe-OFET with and without PMMA coating. j) Optical communication mode with various bending radius. k) Conversion of light signals to digital signals of "0 100 0110" and "0 100 0100." l) Schematics of binary code translation.

maintain stable operation under continuous bending. Due to the suppression of the persistent photoconductivity effect, the optimized photodetector exhibits improved photoresponse speed and enhanced detection sensitivity, demonstrating application potential in real-time optical communication. As evidenced in

Figure 3j-1, the device achieves optical-to-digital signal conversion under mechanical bending conditions. Figure 3k illustrates photocurrent curves corresponding to two-byte input signals "01 000 110" and "01 000 100," which are decoded into the alphabetical characters "F" and "D" through binary code

www.advancedsciencenews.com



16163028, 0, Downloaded from https://advanced.onlinelibrary.wiley.com/doi/10.1002/adfm.022508765 by Fudatu University, Wiley Online Library on [28.09/2025]. See the Terms and Conditions (https://onlinelibrary.wiley.com/terms-and-conditions) on Wiley Online Library for rules of use; OA arctices are governed by the applicable Creative Commons Licenses

www.afm-journal.de

conversion (Figure 31). These results provide a practical solution for implementing photodetectors in ultraviolet optical communication applications.

2.4. Electrical Properties and Nonvolatile Characteristics of Fe-OFET

The electrical properties of Fe-OFET were measured under darkness at room temperature. The polarization characteristics of ferroelectric polymer P(VDF-TrFE) film were confirmed using a capacitor configuration of Au/P(VDF-TrFE)/Au layers, as shown in the inset of Figure 4a. The hysteresis loop of 400 nm-thick P(VDF-TrFE) film demonstrates a polarization switching voltage of 30 V and a remnant polarization (P_r) of 9 μ C cm⁻². Utilizing P(VDF-TrFE) as a dielectric layer, the transfer characteristic curve of the Fe-OFET exhibits typical p-type conduction with an on/off ratio of 105 (Figure 4b). The large hysteresis window (18 V) observed is attributed to the ferroelectric polarization switching process during the gate voltage (V_{o}) sweep range from -45 V to 45 V. When a positive V_{α} exceeding 22 V, the device enters an off-state, suppressing the dark current to as low as $\approx 10^{-12}$ A at a drainsource voltage (V_{ds}) of 0.1 V. Under zero gate voltage and dark environment, the output and photo-switching characteristics for the different polarization states are shown in Figure 4c; Figure S13 (Supporting Information), respectively. These states are defined as P up state (upward polarization) and P down state (downward polarization), based on the electrostatic field generated by the remnant polarization of P(VDF-TrFE), which are achieved by poling P(VDF-TrFE) with V_g pulse of -40 and 40 V, respectively. In the P up state, I_{ds} is suppressed to $\approx 5 \times 10^{-12}$ A at V_{ds} = 0.1 V. Conversely, the P down state exhibits a high channel current due to that thermionic and drift/diffusion dominate channel current. [47,48] Therefore, the local ferroelectric field, derived from the remnant polarization, can fully deplete or accumulate carriers in the hybrid layered organic channel. Figure 4d–f illustrates three scenarios with corresponding energy band diagrams for the Fe-OFET. For the band diagrams of different states, contact barriers between C8-BTBT/MoO3 and MoO3/electrodes are considered. E_f, HOMO, and LUMO are the Fermi level energy, highest occupied molecular orbital and lowest unoccupied molecular orbital of C8-BTBT, respectively. In the initial fresh state, the dipoles within the P(VDF-TrFE) film are randomly oriented. After polarization in the P up or P down directions, the dipoles tend to be ordered in the same orientations. This alignment generates a local ferroelectric field, which modulates carrier distribution in the channel and causes a nonlinear shift in the Fermi level. This mechanism underpins the modulation functionality of the Fe-OFET, enabling precise control over its electronic properties.

Based on nonvolatile properties of devices, integrating memory functionality enables Fe-OFET to achieve logic memory. To assess the storage properties, the write and erase operations were performed via alternating $V_{\rm g}$ pulses as exhibited in Figure 4g. Two logic states were read under $V_{\rm ds}=0.1$ V and confirmed through current dynamic processes. A positive $V_{\rm g}$ pulse ($V_{\rm g}=40$ V) set the device to logic "0", corresponding to a low current level ($\approx\!10^{-12}$ A). Conversely, applying a negative pulse reversed ferroelectric polarization, switching the device to logic "1" with a high current of $\approx 10^{-8}$ A (Figure 4h). Initial endurance loss

during the first 20 cycles was due to incomplete charge compensation and carrier trapping. However, stable switching between the two logic states was recorded after 20 cycles, indicating fatigue-free characteristics. Retention time is another critical metric for non-volatile memory. To investigate this parameter, the as-fabricated devices are set/reset with pulse voltages of \pm 40 V, and then the corresponding states were read at a 2 s interval. Figure 4i shows that two distinct states with a high current ratio (>10⁴) were maintained for over 4×10^3 s without significant degradation, confirming robust nonvolatile storage performance. Variation of the memory window with bending cycles was also assessed as shown in Figure 4j. Hysteresis window narrowed by ≈10% after bending 500 cycles, primarily due to slight morphology damage from mechanical stress. However, the memory window retained 90% of its original value even after 1000 bending cycles, demonstrating exceptional bending resistance. Figure 4k-l further confirms that high/low resistance state remained stable after 1000 cycles, with minimal cycle-to-cycle variability. For retention characteristic after the bending cycles, the two logic states with a high ratio of 10^4 persisted over 4×10^3 s. Inspired by the biological vision system, in situ image memory is simulated, that in situ storage at the location of the signal acquisition (Figure S14, Supporting Information). A 3×4 array units were constructed to demonstrate the cooperation of photo-sensing and data storage. Owing to the polarization characteristics of the ferroelectric layer, binary coding in the array units can be retained for extended periods or reprogrammed via gate voltage. This design integrating photodetection with data storage, although lacking weight updating function, that is, "learning" behavior, highlights longterm "memory" function for light signals, which is challenging for many photonic synaptic devices.[49,50]

2.5. Synaptic Function Emulation and Neuromorphic Computing

The integration of ferroelectric materials in Fe-OFETs demonstrates promising capabilities for neuromorphic computing through electric modulation and nonvolatile polarization mechanisms. Figure 5a shows the excitatory post-synaptic currents (EPSC) behaviors of Fe-OFET in response to a gate voltage pulse at a reading voltage of $V_{ds} = 0.5$ V. The postsynaptic neurons to excite behaviors originated from polarization changes within the ferroelectric domains. Upon application of a negative gate voltage pulse ($V_g = -10 \text{ V}$, 50 ms), partial downward polarization of the P(VDF-TrFE) domains occurs, resulting in a transient increase in channel current followed by relaxation to the initial state. According to the equation of energy consumption (E_c) given by E_c = $V_{read} \times I_{peak} \times t$, where V_{read} represents the drain voltage, I_{peak} represents the spike peak current, and t is the spike duration time. The E_c per spike is ≈ 85 pJ, which is comparable to those of most reported ferroelectric-based artificial synapses (Table S2, Supporting Information). Furthermore, shortening pulse duration and reducing readout voltage can serve as an effective strategy to optimize device energy consumption. In particular, moderately reducing the read-out voltage in circuits can achieve power consumption reduction without substantially compromising key performance metrics of artificial synaptic devices, such as state number, dynamic range, and nonlinearity. Paired-pulse facilitation (PPF), a fundamental synaptic plasticity mechanism in

16163028, 0, Downloaded from https://advanced.onlinelibrary.wiley.com/doi/10.1002/adfm.202508765 by Fudan University, Wiley Online Library on [28/09/2025]. See the Terms and Conditions (https://onlinelibrary.wiley.com/terms

and-conditions) on Wiley Online Library for rules of use; OA articles are governed by the applicable Creative Commons License

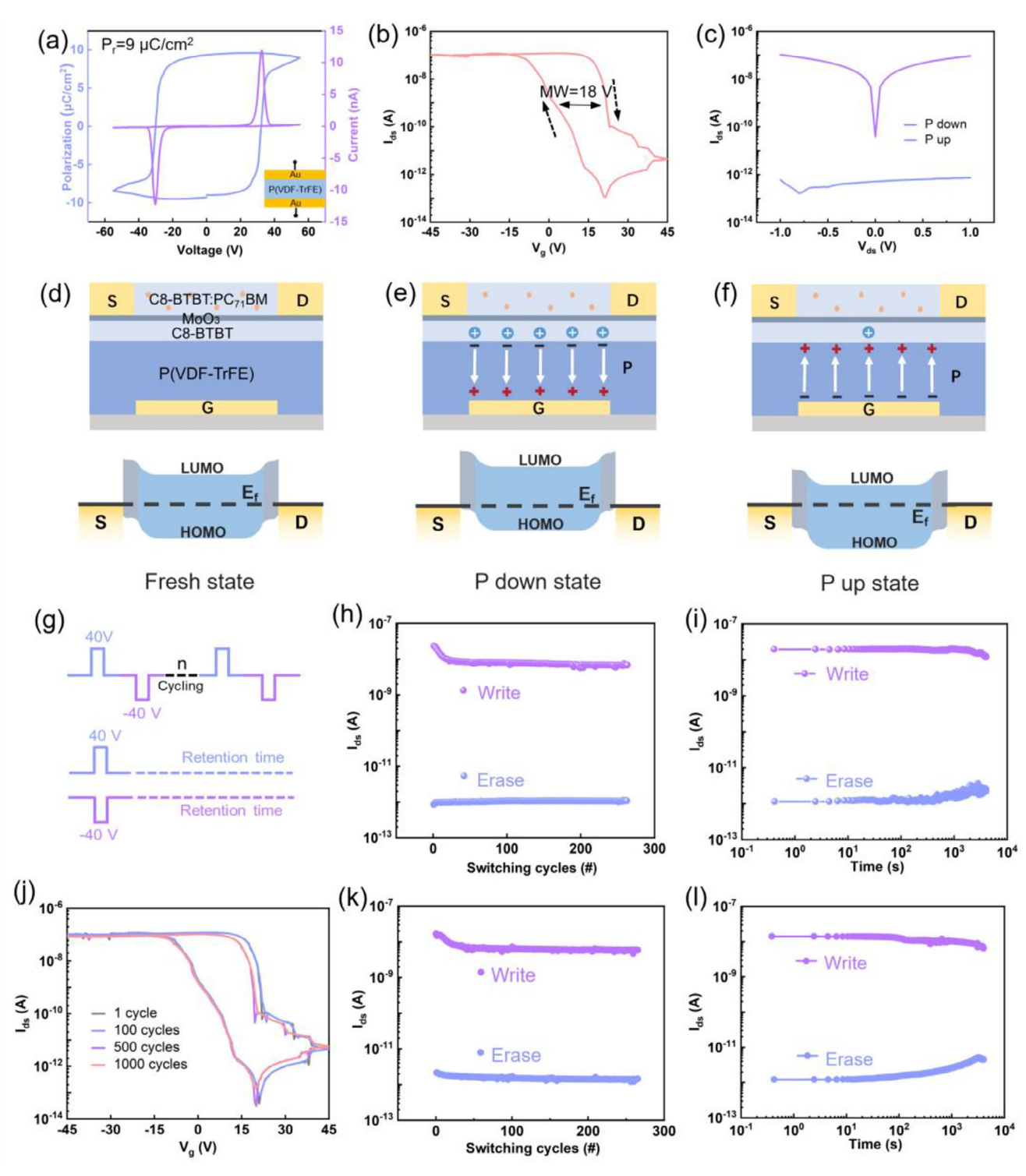


Figure 4. a) Hysteresis loop of the P(VDF-TrFE) ferroelectric film with a thickness of 400 nm. b) Transfer characteristics ($I_{ds}-V_g$) curve of Fe-OFET under dark environment. c) Output characteristic ($I_{ds}-V_{ds}$) curves at up and down polarization states of ferroelectric layer. d–f) The structure diagram of devices and equilibrium energy band diagrams of three different ferroelectric polarization states. g) Programmed gate voltage pulse sequences are performed to test the endurance and retention characteristics of the device. h) Endurance cycle measurement by applying pulse voltages of \pm 40 V under reading voltage of $V_{ds} = 0.1$ V. i) Retention time testing for write and erase operations. j) Transfer characteristics ($I_{ds}-V_g$) curves after bending cycles. k) Endurance cycle measurement and l) retention time testing after 1000 bending cycles.

16163208, 0, Downloaded from https://advanced.onlinelibrary.wiley.com/doi/10.1002/adfm.022508765 by Fudau University. Wiley Online Library on [2809/2025]. See the Terms and Conditions (https://onlinelibrary.wiley.com/terms-and-conditions) on Wiley Online Library for rules of use; OA articles are governed by the applicable Creative Commons Licenses

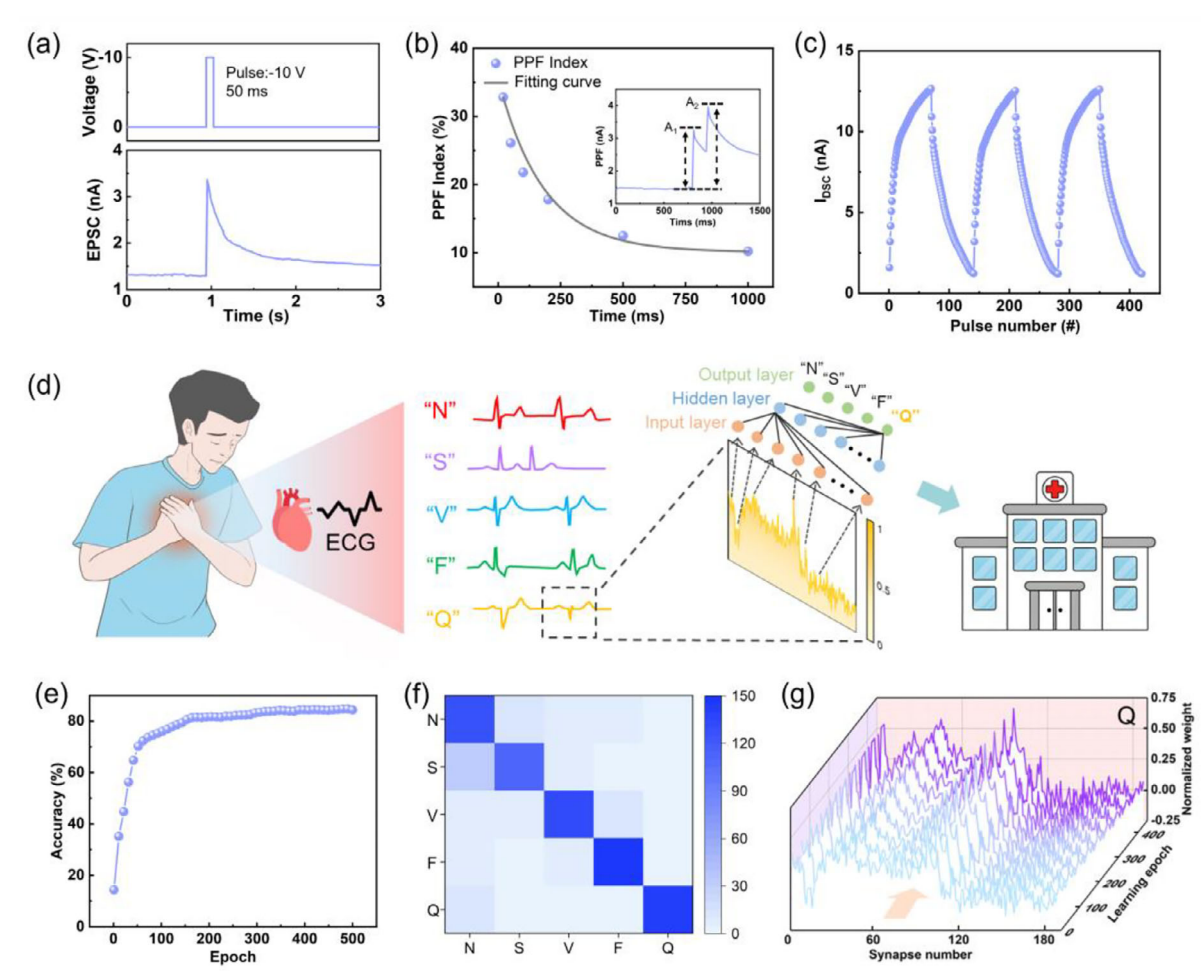


Figure 5. a) EPSC behaviors of Fe-OFET in response to gate voltage pulse at reading voltage of $V_{ds} = 0.5 \text{ V}$ b) PPF property of devices under different pulse intervals. c) Potentiation and depression of synaptic weight update with an incremental pulse scheme. d) Fe-OFET as an information-processing component to analyze ECG signals and display the categorizing results. e) Recognition accuracy and f) Confusion matrix for 5 classes of ECG under 500 epochs. g) Weight updating process for "Q" class during 500 learning epochs.

biological systems, manifests when the synaptic response to a second stimulus is enhanced due to the temporal proximity of two successive pulses. The PPF characteristics of the devices across various pulse intervals are demonstrated in Figure 5b. The PPF index, quantifying the temporal dependence of this facilitation, is expressed as:

$$PPF = (A_2 - A_1) / A_1 \times 100\% \tag{1}$$

where A₁ and A₂ represent the post-synaptic currents induced by the first and second pulses, respectively. The pulse intervaldependent decay of the PPF index exhibits a biphasic decay pattern, comprising rapid and slow components, which can be mathematically described by a double exponential decay function:

$$\gamma = C_0 + C_1 exp\left(-\Delta t/\tau_1\right) + C_2 exp\left(-\Delta t/\tau_2\right)$$
 (2)

Here, C_0 represents the PPF index as the pulse interval approaches infinity, C_1 and C_2 denote the initial facilitation

magnitudes of the rapid and slow phases, respectively, and τ_1 and τ_2 denote their characteristic relaxation times. The experimental data, as illustrated in Figure 5b, demonstrate excellent agreement with this decay function. The observed decay of the PPF index with increasing Δt substantiates the device's capability for temporal information processing, a crucial feature for neuromorphic computing applications. To evaluate the device's analog weight modulation capabilities, Figure 5c presents its potentiation and depression synaptic weight update under an incremental pulse scheme. The application protocol consisted of 70 consecutive negative pulses (-10 V, 50 ms) followed by 70 consecutive positive pulses (10 V, 50 ms) at the gate electrode, repeated for three complete cycles. This testing reveals consistent and symmetric weight updates, with the bidirectional weight modulation responding to gate voltage polarity. These characteristics further substantiate the device's suitability for neuromorphic computing implementations.

As a proof of concept, we demonstrated the application of our Fe-OFET serves as a wearable and intelligent healthcare device for real-time diagnosis for personalized healthcare by

www.afm-journal.de

16163028, 0, Downloaded from https://advanced.onlinelbtarry.wiley.com/doi/10.1002/adfm.022508765 by Fudau University, Wiley Online Library on [2809/2025]. Sethe Terms and Conditions (https://onlinelibrary.wiley.com/terms-and-conditions) on Wiley Online Library for uses of use; OA arctices are governed by the applicable Creative Commons License

processing complicated physiological signals like ECG waveforms from patients with arrhythmia (Figure 5d). ECGs can be used effectively to monitor the health of the cardiovascular system. The subtle morphological similarities between ECG waveforms present significant challenges in accurate waveform categorization and real-time diagnostic interpretation. In ECG classification based on a heartbeat dataset, normal sinus rhythm is designated as "Normal" (N), while arrhythmic abnormalities are categorized into classes "S", "V", "F", or "Q" by different waveforms and morphologies.^[51] To interpret the ECG signals, we utilized shape-related features of each waveform extracted from the ECG heartbeat categorization dataset.^[52] The preprocessing involved segmentation of each ECG waveform into 187 sequential electrical potentials, followed by amplitude normalization. We implemented a two-layer neural network architecture for Q-class recognition, comprising 187 input neurons, 128 hidden layer and 5 output neurons, forming a fully connected neural network. Each electrical potential in the ECG waveform was fed to the corresponding input synapse, and the back-propagation algorithm was employed to calculate the mapped weight values.

The artificial neural network was trained using 3200 patterns in the training dataset, with performance validation conducted on an independent testing dataset of 800 samples. Our Fe-OFETbased implementation achieved ≈85% recognition accuracy under 500 training epochs (Figure 5e). The classification accuracy of the five classes can be visually monitored through the confusion matrix. The deeper the color on the diagonal, the higher the recognition accuracy (Figure 5f). The mapping image visualization of class "Q" demonstrated progressive improvement from 0 to 500 training cycles, indicating successful learning convergence and enhanced discrimination capability (Figure 5g). The learning processes from 0 to 500 epochs of other ECG waveforms are provided in Figure S15 (Supporting Information). Neuromorphic computing facilitates accurate ECG classification, holding promise for improved medical diagnostics and health monitoring.

To further evaluate the scalability and broader applicability of Fe-OFET-based neuromorphic systems, we implemented handwritten digit recognition using the MNIST database (Figure \$16, Supporting Information). The network achieved a classification accuracy of 91% on MNIST patterns, exceeding the recognition accuracy observed in ECG waveforms classification. This superior performance on MNIST can be attributed to the larger training dataset available, suggesting that the ECG recognition accuracy could potentially be enhanced through training with an expanded ECG signal dataset. These results demonstrate the versatility of Fe-OFET architectures in handling diverse pattern recognition tasks. This study advances the development of multimode signal processing, offering a path toward more efficient and compact devices.

3. Conclusion

In this work, we demonstrate ferroelectric-gated organic fieldeffect transistors for multimode signal processing. The device combines a ferroelectric polymer P(VDF-TrFE) as the gate dielectric with a photoactive C8-BTBT:PC71BM layer, and an ultrathin MoO3 interlayer. The hybrid-layered channel with organic molecule modification enables enhanced exciton dissociation, suppressed electron-hole recombination, and improved charge transport. The ferroelectric polarization-induced conductance modulation exhibits robust non-volatile memory and prolonged retention time. Furthermore, Fe-OFET as a wearable, intelligent healthcare device, is capable of real-time diagnosis through the processing of complex ECG signals. This work highlights the potential of the Fe-OFET as a platform for multimode signal processing, offering a multifunctional integration paradigm for future portable and wearable applications.

4. Experimental Section

2,7-dioctyl[1]-benzothieno[3,2-b][1]benzothiophene Materials: The (C8-BTBT, ≥98%) was purchased from Aladdin Scientific Corp. The [6,6]-phenyl- C_{71} -butyric acid methyl ester (PC₇₁BM, \geq 99%) and molybdenum trioxide (MoO₃, 99.9%) were bought from Macklin Inc. The poly(vinylidene fluoride-trifluoroethylene) copolymer (P (VDF-TrFE), 70:30 mol%) was bought from Piezotech, Arkema Group. All chemicals were used without further purification.

Device Fabrication: The polyethylene naphthalate (PEN) substrate was sequentially cleaned with deionized water, ethanol, and acetone for 30 min, followed by nitrogen drying. Prior to coating with the polymer film, the patterned gate electrode (Cr/Au) was deposited using vacuum evaporation. The preparation process of the multilayer film is shown in Figure S1 (Supporting Information). The P(VDF-TrFE) film was spin-coated onto the substrate and annealed at 135 °C for 3 h. Subsequently, C8-BTBT and MoO₂ films were deposited on the P(VDF-TrFE) layer via thermal evaporation. The solution of C8-BTBT:PC71BM obtained by dissolving 0.5 wt.% C8-BTBT and 0.02 wt.% PC71BM in chlorobenzene solvent was applied by improved drop-casting to form a uniform film. The source and drain electrodes (Cr/Au) were deposited on the top of the film by vacuum evaporation. PMMA solution (10 mg mL⁻¹) was spin-coated onto the device surface at 4000 rpm for 40 s, followed by annealing at 80 °C for 10 min to form a protective thin film.

Instrumentation and Test Conditions: The X-ray diffraction (XRD) patterns of the P(VDF-TrFE) and C8-BTBT films were measured using an X-ray diffractometer (Bruker D8). Photoluminescence (PL) spectra were recorded with a Renishaw in Via-Qontor Raman microscope equipped with a 325 nm laser. Absorption spectra were obtained using an ultravioletvisible spectrophotometer (Hitachi, U-3900H). X-ray photoelectron spectroscopy (XPS) was performed to analyze the chemical composition using a Thermo Scientific Escalab 250Xi. Focused ion beam (FIB) was carried out with a FEI Scios 2 HiVac system. Transmission electron microscopy (TEM) and energy-dispersive X-ray spectroscopy (EDS) mapping were conducted using a FEI Talos F200X G2 instrument. The electrical and optoelectronic measurements were performed using a Keithley 4200-S semiconductor test system, equipped with a 75 W xenon lamp capable of continuously tunable wavelengths.

Neuromorphic Computing for ECG and MNIST Pattern Recognition. Two-layer multilayer perceptron neural network simulations based on Fe-OFET were performed using the MNIST handwritten dataset and ECG heartbeat categorization dataset, which was preprocessed by M. Kachuee from the MIT-BIH Arrhythmia Dataset.

Supporting Information

Supporting Information is available from the Wiley Online Library or from the author.

Acknowledgements

The work was supported by the National Natural Science Foundation of China (Grant Nos. 52425308, 62374035, and 92263106) and the China

___ MATERIALS

16163028, 0, Downloaded from https://advanced.onlinelibrary.wiley.com/doi/10.1002/adfm.202508765 by Fudan University, Wiley Online Library on [28/09/2025]. See the Terms and Conditions

(https://onlinelibrary.wiley.com/terms

-and-conditions) on Wiley Online Library for rules of use; OA articles are governed by the applicable Creative Commons License

Postdoctoral Science Foundation (2023M730611). The authors acknowledge Qichao Zhang for his support in the construction of the artificial neural network architecture.

Conflict of Interest

The authors declare no conflict of interest.

Data Availability Statement

The data that support the findings of this study are available from the corresponding author upon reasonable request.

Keywords

ferroelectric materials, hybrid-layered organic field-effect transistor, neuro-morphic computing, photodetector

Received: April 7, 2025 Revised: July 19, 2025 Published online:

- D. Jayachandran, R. Pendurthi, M. U. K. Sadaf, N. U. Sakib, A. Pannone, C. Chen, Y. Han, N. Trainor, S. Kumari, T. V. Mc Knight, J. M. Redwing, Y. Yang, S. Das, *Nature* 2024, 625, 276.
- [2] F. Zhou, Y. Chai, Nat. Electron. 2020, 3, 664.
- [3] X. Li, S. Li, J. Tian, Q. Chen, Adv. Funct. Mater. 2023, 34, 2306486.
- [4] Z. Zhao, Z. Wang, J. Xu, P. Zhao, J. Wang, Y. Wang, W. Zhang, C. Li, H. Cui, J. Wang, Y. Zhang, J. Sun, Y. Pei, Z. Guo, Y. Faraj, J. Chen, S. Li, X. Yan, Adv. Funct. Mater. 2024, 34, 2406666.
- [5] T. Lu, J. Xue, P. Shen, H. Liu, X. Gao, X. Li, J. Hao, D. Huang, R. Zhao, J. Yan, M. Yang, B. Yan, P. Gao, Z. Lin, Y.i Yang, T.-L. Ren, Sci. Adv. 2024, 10, eadp0174.
- [6] F. Cao, Z. Hu, T. Yan, E. Hong, X. Deng, L. Wu, X. Fang, Adv. Mater. 2023, 35, 2304550.
- [7] X. Liu, D. Wang, W. Chen, Y. Kang, S. Fang, Y. Luo, D. Luo, H. Yu, H. Zhang, K. Liang, L. Fu, B. S. Ooi, S. Liu, H. Sun, *Nat. Commun.* 2024, 15, 7671.
- [8] P. Wang, W. Xue, J. Zeng, W. Ci, Q. Chen, B. Lv, R. Yang, Y. Liu, G. Liu, X. Xu, Adv. Funct. Mater. 2024, 34, 2407746.
- [9] Z. Su, Y. Yan, M. Sun, Z. Xuan, H. Cheng, D. Luo, Z. Gao, H. Yu, H. Zhang, C. Zuo, H. Sun, Adv. Funct. Mater. 2024, 34, 2316802.
- [10] H. Huang, X. Liang, Y. Wang, J. Tang, Y. Li, Y. Du, W. Sun, J. Zhang, P. Yao, X. Mou, F. Xu, J. Zhang, Y. Lu, Z. Liu, J. Wang, Z. Jiang, R. Hu, Z. Wang, Q. Zhang, B. Gao, X. Bai, L. Fang, Q. Dai, H. Yin, H. Qian, H. Wu, Nat. Nanotechnol. 2024, 20, 93.
- [11] Y. Zhu, Y. Wang, X. Pang, Y. Jiang, X. Liu, Q. Li, Z. Wang, C. Liu, W. Hu, P. Zhou, *Nat. Commun.* 2024, 15, 6015.
- [12] J.-Y. Chen, D.-L. Yang, F.-C. Jhuang, Y.-H. Fang, J.-S. Benas, F.-C. Liang, C.-C. Kuo, Adv. Funct. Mater. 2021, 31, 2105911.
- [13] B. Jeong, P. Gkoupidenis, K. Asadi, Adv. Mater. 2021, 33, 2104034.
- [14] B. H. Jeong, J. Park, D. Kim, J. Li, I. H. Jung, H. J. Park, Adv. Opt. Mater. 2023, 12, 2301652.
- [15] R. Yu, L. He, C. Gao, X. Zhang, E. Li, T. Guo, W. Li, H. Chen, Nat. Commun. 2022, 13, 7019.
- [16] F. Zhou, Z. Zhou, J. Chen, T. H. Choy, J. Wang, N. Zhang, Z. Lin, S. Yu, J. Kang, H.-S. P. Wong, Y. Chai, Nat. Nanotechnol. 2019, 14, 776.
- [17] Y. Gong, R. Duan, Y. Hu, Y. Wu, S. Zhu, X. Wang, Q. Wang, S. P. Lau, Z. Liu, B. K. Tay, *Nat. Commun.* **2025**, *16*, 230.

- [18] C. Pan, C.-Y. Wang, S.-J. Liang, Y. Wang, T. Cao, P. Wang, C. Wang, S. Wang, B. Cheng, A. Gao, E. Liu, K. Watanabe, T. Taniguchi, F. Miao, Nat. Electron. 2020, 3, 383.
- [19] A. Ram, K. Maity, C. Marchand, A. Mahmoudi, A. R. Kshirsagar, M. Soliman, T. Taniguchi, K. Watanabe, B. Doudin, A. Ouerghi, S. Reichardt, I. O'Connor, J.-F. Dayen, ACS Nano 2023, 17, 21865.
- [20] G. Wu, X. Zhang, G. Feng, J. Wang, K. Zhou, J. Zeng, D. Dong, F. Zhu, C. Yang, X. Zhao, D. Gong, M. Zhang, B. Tian, C. Duan, Q.i Liu, J. Wang, J. Chu, M. Liu, Nat. Mater. 2023, 22, 1499
- [21] R. Peng, Y. Wu, B. Wang, R. Shi, L. Xu, T. Pan, J. Guo, B. Zhao, C. Song, Z. Fan, C. Wang, P. Zhou, S. Fan, K. Liu, Nat. Electron. 2023, 6, 852
- [22] Y. Cai, Y. Jiang, C. Sheng, Z. Wu, L. Chen, B. Tian, C. Duan, S. Xiong, Y. Zhan, C. Cong, Z.-J. Qui, Y. Qin, R. Liu, L. Hu, npj Flex. Electron. 2023, 7, 29.
- [23] C. Luo, Y. Zhang, W. Shuai, K. He, M. Li, R. Tao, D. Chen, Z. Fan, B. Zhang, X. Zhou, J.-Y. Dai, G. Zhou, X. Lu, J.-M. Liu, Sci. China Mater. 2023, 66, 2372.
- [24] X. Fu, T. Li, B. Cai, J. Miao, G. N. Panin, X. Ma, J. Wang, Q. Li, Y. Dong, C. Hao, J. Sun, H. Xu, Q. Zhao, M. Xia, B. Song, F. Chen, X. Chen, W. Lu, W. Hu, Light, Sci. Appl. 2023, 12, 39.
- [25] K. Asadi, D. M. de Leeuw, B. de Boer, P. W. M. Blom, *Nat. Mater.* 2008. 7, 547.
- [26] G. H. Gelinck, A. W. Marsman, F. J. Touwslager, S. Setayesh, D. M. de Leeuw, R. C. G. Naber, P. W. M. Blom, *Appl. Phys. Lett.* 2005, 87, 092903.
- [27] M. Carroli, A. G. Dixon, M. Herder, E. Pavlica, S. Hecht, G. Bratina, E. Orgiu, P. Samorì, Adv. Mater. 2021, 33, 2007965.
- [28] E. Restuccia, A. Ghobadi, S. Guha, Adv. Mater. Interfaces 2025, 12, 2401035.
- [29] X.-K. Wei, N. Domingo, Y. Sun, N. Balke, R. E. Dunin-Borkowski, J. Mayer, Adv. Energy Mater. 2022, 12, 2201199.
- [30] L. Qi, S. Ruan, Y. J. Zeng, Adv. Mater. 2021, 33, 2005098.
- [31] J. Liu, L. Su, X. Zhang, D. V. Shtansky, X. Fang, Small Methods 2023, 8, 2300319
- [32] P. Wang, J. Li, W. Xue, F. Jiang, L. Shi, F. Zhou, P. Zhou, Adv. Sci. 2023, 11, 2305679.
- [33] W. Ci, W. Xue, P. Wang, W. Yin, X. Wang, L. Shi, P. Zhou, X. Xu, Adv. Funct. Mater. 2023, 34, 2305822.
- [34] Y. Zhao, X. Fan, J. Feng, X. Wang, Y. Wu, B. Su, L. Jiang, Adv. Funct. Mater. 2018. 34. 1800470.
- [35] K. Jinnai, R. Kabe, Z. Lin, C. Adachi, Nat. Mater. 2021, 21, 338.
- [36] L. Tu, Y. Chen, X. Song, W. Jiang, Y. Xie, Z. Li, Angew. Chem., Int. Ed. 2024, 63, 2402865.
- [37] M. Anzola, C. Sissa, A. Painelli, A. A. Hassanali, L. Grisanti, J. Chem. Theory Comput. 2020, 16, 7281.
- [38] M. Xu, C. Wei, Y. Zhang, J. Chen, H. Li, J. Zhang, L. Sun, B. Liu, J. Lin, M. Yu, L. Xie, W. Huang, Adv. Mater. 2023, 36, 2301671.
- [39] R. Roy, C. Brouillac, E. Jacques, C. Quinton, C. Poriel, Angew. Chem., Int. Ed. 2024, 63, 2402608.
- [40] Z. Zhao, Y. Cai, Q. Zhang, A. Li, T. Zhu, X. Chen, W. Z. Yuan, Nat. Commun. 2024, 15, 5054.
- [41] B. Fu, F. Yang, L. Sun, Q. Zhao, D. Ji, Y. Sun, X. Zhang, W. Hu, Adv. Mater. 2022, 34, 2203330.
- [42] S. Duan, T. Wang, B. Geng, X. Gao, C. Li, J. Zhang, Y. Xi, X. Zhang, X. Ren, W. Hu, Adv. Mater. 2020, 32, 1908388.
- [43] H. Zhou, C. Liu, S. Liu, Z. Zhang, S. Sun, W. Xu, X. Ma, J. Wang, Y. Xu, X. Du, S. Y. Jeong, H. Y. Woo, F. Zhang, Q. Sun, Small 2023, 20, 2308216.
- [44] B. Qiu, S. Chen, C. Sun, J. Yuan, X. Zhang, C. Zhu, S. Qin, L. Meng, Y. Zhang, C. Yang, Y. Zou, Y. Li, Sol. RRL 2020, 4, 1900540.
- [45] Z. Fang, C. Liu, X. Li, L. Peng, W. Ding, X. Guo, W. Hou, Adv. Funct. Mater. 2022, 33, 2210010.



www.advancedsciencenews.com



www.afm-journal.de

16163028, 0, Downloaded from https://advanced.onlinelibrary.wiley.com/doi/10.1002/adfm.202508765 by Fudan University, Wiley Online Library on [28/09/2025]. See the Terms

) on Wiley Online Library for rules of use; OA articles are governed by the applicable Creative Commons License

- [46] Y. Gao, Y.a Yi, X. Wang, H. Meng, D. Lei, X.-F. Yu, P. K. Chu, J. Li, Adv. Mater. 2019, 31, 1900763.
- [47] D. Zheng, J. Wang, W. Hu, L. Liao, H. Fang, N. Guo, P. Wang, F. Gong, X. Wang, Z. Fan, X. Wu, X. Meng, X. Chen, W. Lu, *Nano Lett.* 2016, 16, 2548.
- [48] X. Wang, P. Wang, J. Wang, W. Hu, X. Zhou, N. Guo, H. Huang, S. Sun, H. Shen, T. Lin, M. Tang, L. Liao, A. Jiang, J. Sun, X. Meng, X. Chen, W. Lu, J. Chu, Adv. Mater. 2015, 27, 6575.
- [49] K. Lee, H. Han, Y. Kim, J. Park, S. Jang, H. Lee, S. W. Lee, H. Kim, Y. Kim, T. Kim, D. Kim, G. Wang, C. Park, Adv. Funct. Mater. 2021, 31, 2105596.
- [50] T. Kim, K.-S. Yun, Sci. Rep. 2023, 13, 12583.
- [51] S. Ham, M. Kang, S. Jang, J. Jang, S. Choi, T.-W. Kim, G. Wang, Sci. Adv. 2020, 6, eaball78.
- [52] M. Kachuee, S. Fazeli, M. Sarrafzadeh, 2018 IEEE International Conference on Healthcare Informatics, IEEE, New York, NY 2018, p. 443.